

Performance and calibration of the NIKA camera at the IRAM 30m telescope

author list to be given by NIKA-eboard

Address(es) of author(s) should be given

December 20, 2013

Abstract

The New IRAM KID Array (*NIKA*) instrument is a dual-band imaging camera operating with Kinetic Inductance Detectors (KID) cooled at 100 mK. *NIKA* is specially designed to observe the millimeter sky at 1.25 and 2.14 mm from the IRAM 30 m telescope at Pico Veleta. This work presents the performance of the *NIKA* camera prior to its opening to the astrophysical community as an IRAM instrument in early 2014. In particular, this is a test-bench for the final *NIKA2* instrument to be installed at the end of 2015. The last *NIKA* observation campaigns on November 2012 and June 2013 have been used to evaluate this performance and to improve the control of systematic effects. We discuss the dynamical tuning of the Read-Out Electronics to optimize the KID working point with respect to background changes and the new technique of atmospheric absorption correction. These modifications improve significantly the overall linearity, sensitivity and absolute calibration performance of *NIKA*. This is proved on observations of point-like sources for which we obtain a sensitivity (averaged over all valid detectors) of 40 and 14 mJy $\text{s}^{1/2}$ for best weather conditions for the 240 and 140 GHz arrays, respectively. *NIKA* observations of well known extended sources (DR21 complex, Cygnus A and the Horsehead nebula) are presented and we demonstrate *NIKA* can reconstruct angular scales up to one arcminute. This performance makes the *NIKA* camera a competitive astrophysical instrument as shown in a companion paper where we present first observations of the tSZ effect on cluster of galaxies.

thermal

1. Introduction

New challenges in millimetre wave astronomy require instruments with a high sensitivity, a high resolution as well as large mapping speed. To achieve such goals, the development of a new generation of array of detectors is needed, since current individual detectors, such as high impedance bolometers (Tauber & Planck Collaboration 2012), are already photon noise limited both for space and ground observations. One of the proposed technological solutions is the use of Kinetic Inductance Detectors (KID) that allow for a large multiplexing factor (up to 400 pixels, Bourrion et al. (2012a)), with a frequency domain read-out and an accessible manufacturing (Doyle et al. (2007), Barends et al. (2008)). This technological solution has been selected for the *NIKA* project (Monfardini et al. (2012)) that aims at constructing a dual-band millimeter camera for observations at the 30m IRAM telescope (Pico Veleta, Spain). Within this context, the *NIKA* camera is a three-hundred-pixel instrument aimed as a first demonstration on the sky of a KID technology application and a prototype in preparation for the development of *NIKA* 2, the full-blown instrument planned for the end of 2015. The goals of the *NIKA* instrument are to perform simultaneous observations in two millimeter bands (1.25 mm and 2.14 mm) of mJy point sources as well as to map faint extended continuum emission up to about 5 arcmin scale with a diffraction-limited resolution and a background-limited performance. Such observational requirements will lead the *NIKA* instrument to be a science driver in several astrophysical fields as the follow-up of Planck clusters (Planck Collaboration et al. (2013)) via the Sunyaev-Zel'dovich effect, high red-

shift sources and quasars, early stages of star formation and nearby galaxies emission. The *NIKA* camera is now open to public observations at the beginning of 2014.

Previous observational campaigns with the *NIKA* have revealed several technical aspects that limited the sensitivity of detectors and the overall calibration accuracy of the instrument. The first one concerns the working point of the detectors that is evolving with time, due to varying atmospheric conditions, thus producing a loss of response. A dynamical tuning of the Read-Out Electronics has been developed in order to optimize the KID working point between two different sky observations. The second one deals with the atmospheric absorption correction for which we have developed a procedure in order to use the *NIKA* instrument itself as a tau-meter.

These improvements were implemented for the last two technical time observational campaigns that took place on November 2012 and June 2013 hereafter called Run5 and Run6, and we report here about the improvements over the overall linearity, sensitivity and absolute calibration performance of *NIKA*.

This article is organized as follow: we first give a review of the main characteristics of the *NIKA* instrument, focusing on the instrumental improvements with respect to the previous observational campaigns (Sec. 2 and 3). In Section 4 we describe the sky observations made with *NIKA* that allowed to characterise the focal plane. In Section 5 we give a short description of the reduction pipeline we used to analyse the data. In Section 6 we describe the atmospheric absorption correction method. In Section 7, we present the final performance of *NIKA* accounting for the instrumental

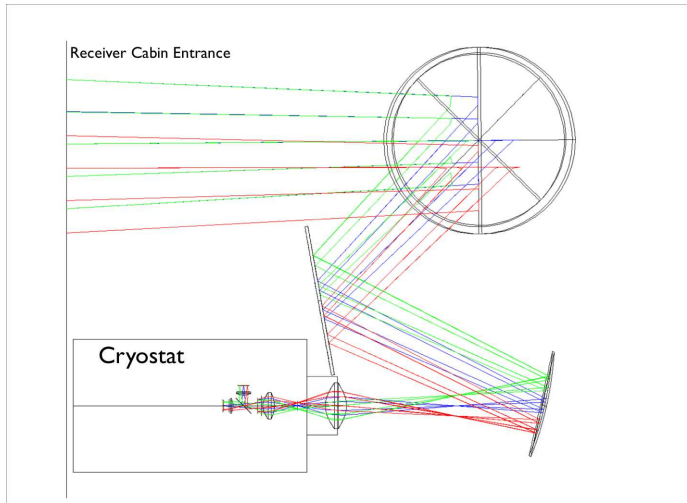


Figure 1. Snapshot from the Zemax simulation used to optimize the optical system of NIKA: the image shows the ray tracing from the entrance of the receiver cabin of the 30m telescope (which is simulated but not shown on the image), view from the elevation axis (which is symbolized by the big circles and contain the 2 mirrors of the Nasmyth system). The NIKA cryostat and entrance nose are symbolised by the rectangles.

noise equivalent flux density (NEFD) calculated on point sources. Finally in Section 8 we show observations of points like and extended sources of the last November 2012 (run5) and June 2013 (run6).

2. The NIKA Instrument

Cooling the two KID arrays at about 100 mK is the major requirement that drives the architecture of the *NIKA* instrument. This is achieved by a 4 K cryocooler and a closed-cycle ^3He - ^4He dilution. The optical coupling between the telescope and the detectors is made by warm aluminum mirrors and cold refractive optics. The optics contain in particular a flat mirror at the top of the cryostat, an off-axis biconic-polynomial curved mirror, a 300K window lens, a field stop, a 4K lens, an aperture stop, a dichroic, a 100mK lens and two band-defining filters in front of the back-illuminated KID arrays, which have a backshort matching the corresponding wavelength. A view of the optics of the *NIKA* instrument and the coupling with the 30 m telescope is presented in Fig. 1. All the elements presented on this figure are real optical elements except for the vertical segment showing the entrance of the receiver cabin and the vertical segments inside the cryostat (field and pupil diaphragms, filters, dichroic and detectors arrays).

The rejection of unwanted emission of the sky and the telescope is achieved by using a combination of low-pass metal mesh filters, placed at different cryogenic stage in order to minimize the thermal loading of the instrument. This determines the shape, width and position of each NIKA band. Spectral characterisation of the NIKA bandpass was performed using a Martin-Puplett interferometer allowing to recover the spectral performance of each pixel of the two NIKA channels providing good data of few % detection level

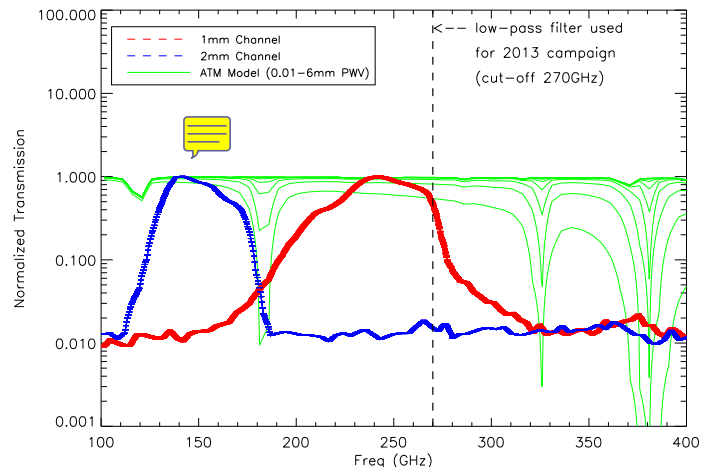


Figure 2. NIKA bandpasses. The bandpass of the 1.25 mm channel (resp. 2.14 mm) is shown in red (resp. blue). The bandpasses are averaged over all valid pixels, with dispersion (rms) of 2% at 1.25 mm and 1% at 2.14 mm. The ATM model calculated for different water vapor contents is presented in ~~purple~~ green

around the passband. In Fig 2 we present the NIKA bandpasses together with the ATM model calculated for different water vapor contents (Pardo et al. (2002)). According to the Pardo model, the 1.25 mm channel is almost sensitive only to the water vapour emission at 183 GHz rather than 2.14 mm channel, sensitive only to the roto-vibrational emission line of dioxygen at 119 GHz. Changing the precipitated water vapour content (PWV) in the ATM model, we can derive the expected opacities integrated into the NIKA channels. The ratio between the opacities derived for 1.25 mm and 2.14 mm channels is obtained not only according to the pseudo continuum emission of the atmosphere (proportional to ν^2) but also taking into account the contribution of the water vapor emission and dioxygen emission. Furthermore, between 2012 and 2013 we changed the optical filter chain by adding a low pass filter with a cut-off at 270GHz. Therefore, we expect to have a different ratio in the opacities at 1.25 mm and 2.14 mm channels between the two campaigns. From the model, we obtain a ratio between the in-band opacities $\tau(2.14\text{mm})/\tau(1.25\text{mm})$ of 0.75 for 2012 campaign and 0.66 for 2013 campaign.

2.1. Detector arrays configurations

The detector arrays are made of Aluminum LEKID based on a Hilbert pattern inductor (Roesch et al. (2012)). The results reported in this paper cover two different observation campaigns at the telescope, with slightly different properties of the two focal planes:

- **Campaign 11/2012.** During this campaign, which is referred to as run 5 in the following, the 2.14 mm array is made of 132 pixels made with a 20 nm thick Al film on a 300 μm HR Silicon substrate. The 1.25 mm array is made of 224 pixels made of a film of the same thickness but on a 180 μm substrate. The cold amplifier of the 240 GHz channel showed an unexpectedly low saturation power, so that we could readout simultaneously only 8

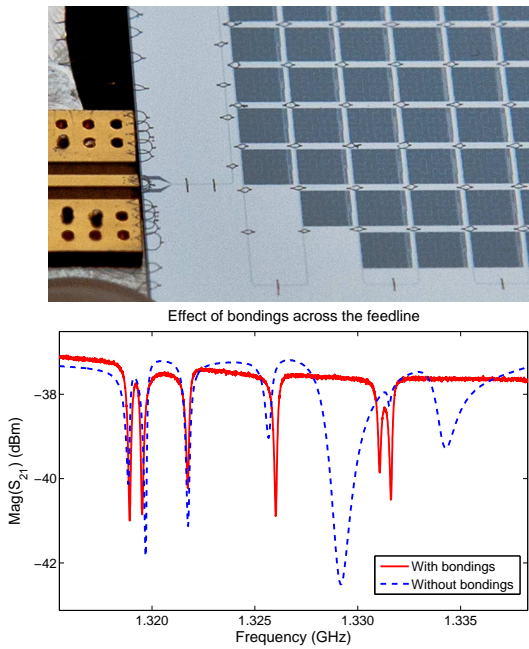


Figure 3. Image of the bondings added across the feedline (top). As can be seen in the frequency sweep carried out before and after adding the bondings (bottom), the depth of the different resonances has become much more uniform, as the coupling of the resonators to the feedline is no longer affected by the presence of standing waves supported by the slotline modes. Such standing waves were also responsible of the larger dips that are observed before adding the bondings and that disappear afterwards.

pixels with the ideal excitation level, or alternatively 90 pixels but with a lower power per tone, resulting in sub-optimal performance. The number of valid pixels were around 100 and 80 for the 2.14 mm and 1.25 mm channels respectively.

- **Campaign 06/2013.** This campaign is referred to as run 6 in the following. For the 2.14 mm channel, we replaced the array with a new one, obtained from a thinner Al film (18nm), and in which we optimized the coupling to the feedline. We also added bondings across the feedline to suppress spurious slotline modes that were affecting the uniformity of the pixel properties, which led to an increase in the number of valid pixels (figure 3). The overall geometry and the pitch between pixels was left unchanged, as was the readout chain. For the 1.25 mm channel, the only intervention was the replacement of the cold amplifier with a new one having a higher power handling. RF filters have also been added on the readout chain to suppress the harmonics of the Local Oscillator from reaching the cold amplifier input. Since we suspected that the optical load on the 1.25 mm array was preventing it from cooling down appropriately, we added in front of it an extra low-pass filter cutting frequencies above 270 GHz, even though this led to the loss of a fraction (roughly XX%) of the power available in the atmospheric window of interest. The number of valid pixels was for this campaign 125 at 2.14 mm and 190 at 1.25 mm, for a total of more than 300 pixels.

For the readout, we used the new NIKEI version 1 electronics, which have worked flawlessly. The boards, described in detail in Bourrion et al. (2012b), are capable of generating up to 400 tones each over a 500MHz bandwidth. This is achieved by using 6 separate FPGAs: five of them generate 80 tones each over a 100MHz band, using five associated DACs. The sixth FPGA acts as a central unit that combines the signal of the other units, appropriately shifting and filtering the different 100MHz sub-bands to finally cover the whole 500MHz available for the frequency comb used to excite the detectors. An analogous, but reversed, process is then applied to the signal acquired by the ADC of the board, which is once again split in 5 different sub-bands treated separately. Each NIKEI v1 board thus allows us to monitor all the 400 tones simultaneously.

Data are acquired at a 22.842 Hz rate, synchronously over the two arrays. Fits files are provided as output, which contain the raw data as well as the resonant frequency of each KID used to set the corresponding excitation tone.

3. REU optimisation procedure

In the standard KID readout scheme, each pixel is excited using a fixed tone at its resonant frequency. The signal transmitted past the detector is compared to a reference copy of the excitation signal to get its in-phase (I) and quadrature (Q) components. From these it is then necessary to estimate the corresponding shift in resonance frequency f_0 of the detector, as this is the physical property directly related to the incoming optical power: $\delta f_0 \propto \delta P_{opt}$ for small values of δP_{opt} (Swenson et al. (2010)). Finding a reliable way to evaluate $f_0(t)$ starting from $I(t)$ and $Q(T)$ represents a challenge, and this is especially true in the case of ground-based experiments, as these have to cope with the effects induced by the variations in atmospheric opacity.

3.1. Modulated Readout

For the NIKA detectors an innovative readout technique has been developed, which has been successfully tested during the 2011 run and adopted for all the following campaigns. The details of this technique are described in Calvo et al. (2013). Briefly, the underlying idea is that of replacing the standard excitation of the detectors, which uses a fixed tone, with a new excitation based on two different frequencies. We achieve this by modulating the Local Oscillator signal between two values, separated by δf_{LO} , in order to generate two tones, one just above ($f_+ = f_0 + \delta f_{LO}/2$) and one just below ($f_- = f_0 - \delta f_{LO}/2$) the detector resonant frequency. The modulation is carried out at about 1kHz, synchronously to the FPGA sampling of the signal. Thus, each raw data point, sent to the acquisition software at a rate of 22.842Hz, is composed by the values $(I(t), Q(t))$ of each pixel as well as the corresponding differential values

$$\left(\frac{dI}{df}(t), \frac{dQ}{df}(t) \right) = \left(\frac{I(f_+) - I(f_-)}{\delta f_{LO}}, \frac{Q(f_+) - Q(f_-)}{\delta f_{LO}} \right) \quad (1)$$

If a variation $(\Delta I(t), \Delta Q(t))$ is observed between successive points, it is possible to estimate the corresponding shift in the resonant frequency, $\Delta f_0(t)$, by projecting $(\Delta I(t), \Delta Q(t))$ along the gradient found using equation 1:

$$\Delta f_0(t) = \frac{(\Delta I(t), \Delta Q(t)) \cdot (dI/df(t), dQ/df(t))}{(dI/df(t), dQ/df(t))^2} \cdot \delta f_{LO} \quad (2)$$

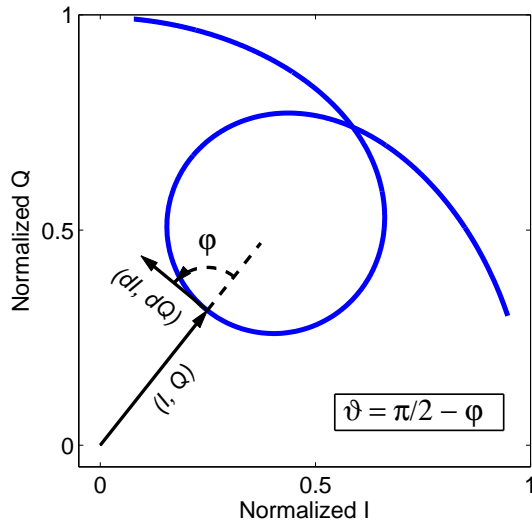


Figure 4. Representation in the I-Q plane of a sweep around a resonance. The measure of the angles ϕ and θ can be carried out for each acquired point thanks to the modulated readout technique. On resonance, one gets $\theta = 0$

We use the name $RFdIdQ$ to refer to this estimate of Δf_0 .

3.2. Automated tuning procedure

The modulated readout technique is the core of a fast and effective method to retune the detectors that we have successfully implemented during the last two campaigns. When operating from ground, the variations in the background load due to the atmosphere can ~~cause~~ vary by a substantial amount, introducing shifts that can be larger than the resonances themselves. This effect must be constantly monitored and, if needed, counterbalanced by changing the excitation tones, in order to always match the resonant frequency of each pixel and to thus keep the detectors near to their ideal working point.

The standard solution is that of performing full frequency sweeps before each on-sky observation, but this leads to a substantial loss of observing time. The new tuning method is simply based on the measurement of the angle ϕ between the vectors (I, Q) and $(dI/df_{LO}, dQ/df_{LO})$, as shown in figure 4. Thus, a single data point is now sufficient to retune the detectors, without recurring to frequency sweeps. This leads to a crucial advantage in terms of observing time, especially in the case of medium and poor weather, in which case as much as 25% of the time was needed for the frequency sweeps used to tune the detectors in the previous runs. Furthermore, in the case of altazimuthal maps, which are always composed of different subscans, the fast tuning method makes it in principle possible to recenter the tones during the time spent by the telescope for changing the direction of its motion at the end of each subscan. Although we still did not make use of this approach, it does not pose any fundamental issue, and might prove highly effective especially in the case of large maps and long integration, in which case the sky conditions can change significantly between the start and the end of an observation.

The tuning process takes place as follows: from the angle ϕ we calculate $\theta = \pi/2 - \phi$, so that the new angle θ

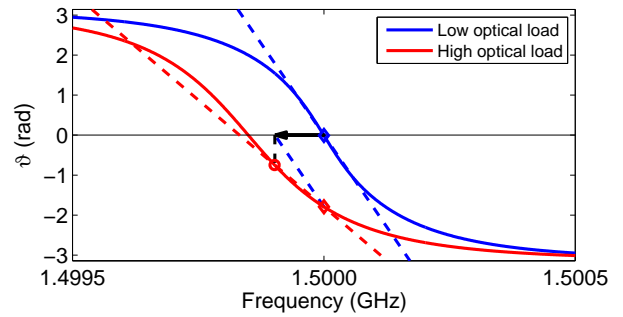


Figure 5. Representation of the tuning technique based on the measure of θ . A sweep (solid line) is carried out to look for the resonances where $\theta = 0$. The tone is fixed at the corresponding frequency (diamond) and the slope is evaluated (dashed line). If the optical load increases, θ changes. From it it is possible to evaluate a correction Δf_0^i (black arrow). The new tone (circle) will be nearer to the actual position to the resonant frequency, f_0^i , and will be used to update the estimated slope of the $\theta(f)$ curve, thus making the iterative tunings more and more accurate.

varies smoothly, decreasing across each resonance from π to $-\pi$. After an initial frequency scan is performed to find the resonances, we fix each excitation tone where $\theta = 0$. At the same time, the slope of the curve $\theta(f)$, which is approximately linear around the resonance, is determined as $\Delta\theta/\Delta f$. Once the tones are fixed, for each tone at frequency f^i it is possible to continuously monitor the value of θ^i . If the corresponding resonant frequency f_0^i shifts, due to changes in optical load, this directly translates in a variation of θ^i , from which it is possible to estimate the actual value of $f_0^i(t)$ as

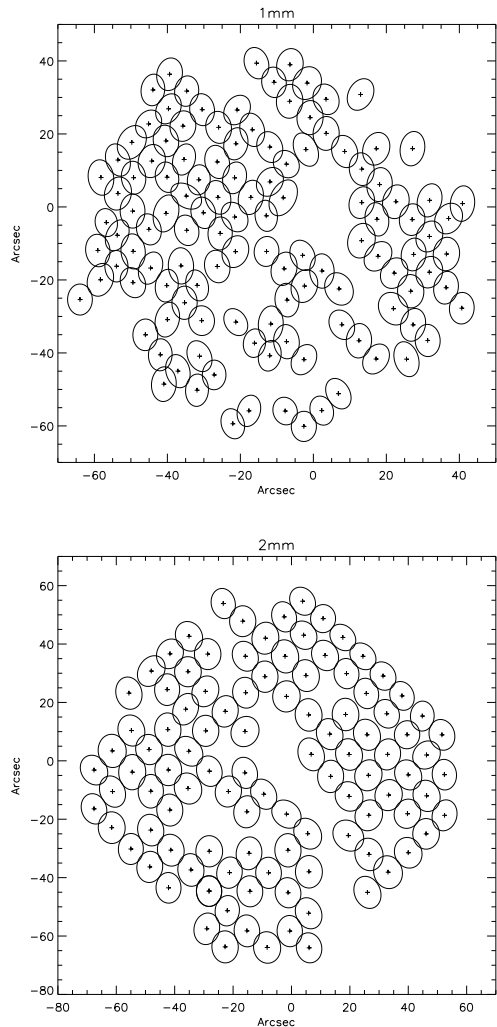
$$f_0^i(t) \simeq f^i - \frac{\theta^i(t)}{\Delta\theta/\Delta f} \quad (3)$$

Although this relationship is not exact, mainly due to the fact that the changes in the optical load affect the $\theta(f)$ relationship and the corresponding value of $\Delta\theta/\Delta f$, the results are very accurate, provided that the shift of the resonance frequency does not exceed the resonance width.

The results can be further improved by iterating the process. For this reason every time that the telescope is not observing we activate an automated tuning procedure. This procedure repeatedly estimates the current value of $f_0^i(t)$ for each detector using equation 3, adjusts the corresponding tone accordingly (figure 5), and updates the coefficient $\Delta\theta/\Delta f$ by measuring the value of θ^i just before and just after changing the frequency f^i . This thus takes into account the changes in the slope of $\theta(f)$, and allows the excitation tone f^i to rapidly converge to the correct resonant frequency $f_0^i(t)$. The procedure is then halted as soon as a new observation starts.

4. Focal plane properties and main beam characterisation

The frequency multiplexing of NIKA prevents us from knowing the pointing direction of each detector on the sky a priori. This has to be determined on astronomical observations. We therefore scan a strong astromical source with the



→ **Figure 6.** Focal planes at 1 and 2mm for run 6.

entire focal plane. The source, typically a planet, is small compared to our beam and can be considered as a point source. It is raster scanned at 35 arcsec/s, and each sub-scan is 420 arcsec long, centered on the source (the source is being tracked by the telescope). A 302 arcsec wide median filter is applied to the detector timelines to subtract atmospheric signal and low frequency correlated electronic noise while preserving the planet signal. These timelines are then projected onto individual maps per detector. A Gaussian elliptical fit is then performed on these maps to derive the beam width of each detector and its pointing offset with respect to the nominal telescope pointing. Knowing the opacity of the sky at this time of observation (cf. sect. 6.2) and the flux of the source, this beam fit also provides a point source photometric calibration for each detector.

As an example, figures 6 and 7 show maps of our 1.24 mm and 2.14 mm focal planes and the distribution of our beam width for 2013 Campaign. calibration source are performed several times accross the campaign to improve on the reconstruction of the pointing. With typically six such scans, we observe a median variation of the dector pointing directions of 3.4 and 3.2 arcsec at 240 and 140 GHz respectively for 2013 observation campaign, even under poor weather conditions with opacities ranging from 0.5 to 0.9.

5. Data Reduction

As discussed in section 3.1 The NIKA data are acquired at 23.842 Hz sampled with individual frequency tone. We recover the in-phase (I) and the quadrature (Q) part of the transfer function of the transmission line + KIDs. Thanks to the use of a modulated Read-Outs electronics and the optimisation procedure (RFdIdQ), we can deduct the variation of the resonant frequency with an improved accuracy. We developed a dedicated reduction pipeline to calibrate, filter and process data onto the maps. The main step of the processing are:

- **Read raw** : this step uploads sky raw data and the main instrument parameters including focal plane reconstruction and atmospheric opacity for each observational scan.
- **Flags** : Bad detectors are flagged based on the fact that the frequency range is not large enough to have a low cross-talk level. Other detectors are flagged depending on the statistical properties of their noise (such as gaussianity, stationarity, noise jumps). Frequency lines produced by the vibration of the cryostat pulse tube are flagged and removed with dedicated filters.
- **Cosmic rays** : We detect glitches in raw data. Since 1.24 mm and 2.14 mm KID arrays are different (in terms of size of the pixels and thickness of the substrate), the rate of observed glitches varies between each other. We observe about 6 glitches/min in 2.14 mm array and about 4 for the 1.24 mm array. The rate of the → **glitches observed** is in pretty good agreement with the expected cosmic ray flux at IRAM telescope (essentially muons with a rate of the order of 2 events/cm²/min). The time response of the KIDs is of the order of hundreds of ms which is negligible compared to the NIKA → **acquisition rate**, therefore all the cosmic rays hits appears only on one single sample. Glitches are removed from the TOD by flagging peaks at 5 sigma level. Then the TOD is interpolated in order to not to perturbate the decorrelation.

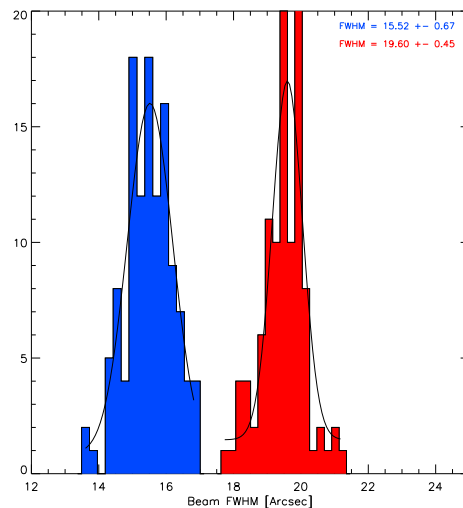


Figure 7. Beam widths at 1.24 and 2.14 mm for 2013 observation campaign.

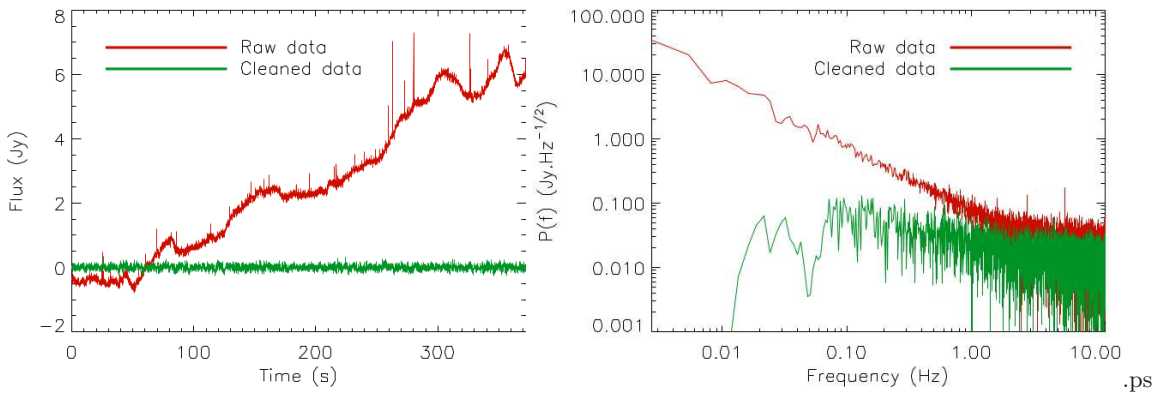


Figure 8. TOD (left) and power spectra (right) for a given detector. TOD before (red) and after (green) the electronic and atmospheric noise decorrelation. I PUT HERE THE TOI PROCESSING FIGURE FROM ADAM ET AL. PAPER. NEED TO BE CHANGED WITH A SIMILAR FIGURE FOR A PLANET OBSERVATION.

- **Calibration of the TOD :** The absolute calibration is applied to these TODs and an opacity correction is performed (see section 6.2).
- **Atmospheric and electronic noise decorrelation :** Depending on the scientific target, three decorrelation methods have been developed :
 - 1) Dual band decorrelation : this is done to recover thermal Sunyaev - Zel'dovich electromagnetic spectrum. See (Adam et al 2013) for more detail.
 - 2) One band Extended source decorrelation : ✓
 - 3) One band point source decorrelation : ✓
- **Map making :** We project and average the signal from all KIDs of a single array on a pixelized map. we subtract the mean value of the projected timeline.

6. Photometric Calibration

The variety of NIKA scientific targets going from thermal SZ observations to dust polarization properties requires a very accurate calibration process able to define as best as possible the impact of systematic errors on the final sky maps. In the following, a list of the principal errors sources that have a direct impact on the total calibration error is presented. In Tab 1, we quantify these contributions.

- **Spectral response :** The band-passes as described in section 2 are obtained as an average of all pixels for each channel. This leads to a contribution to the total calibration error due to the dispersion of the measured band-passes and to the slightly different response of the pixels.
- **Atmospheric absorption correction :** The sky maps are corrected for the atmospheric contribution rescaling the observed signal onto the scale that would be obtained using a detectors outside the atmosphere. This is achieved via the elevation scan technique (*skydip*). The NIKA *skydip* procedure was successfully tested during the two last NIKA observational campaigns and it produced a low level dispersion of the derived opacity at different elevation.
- **Focal plane reconstruction :** In order to understand the pointing direction of each pixel a focal plane reconstruction via planets scan is needed. The accuracy of this technique has been given in section 4
- **Secondary beam fraction :** Planets observations were used to measure individual pixel beams as well

as the focal plane reconstruction. The beam size is obtained by fitting a gaussian on the planets maps. This induces a systematic error in the final calibration which is due to the secondary beams variation with atmospheric opacity.

In the following we discuss in more details the Secondary beam fraction contribution and the atmospheric absorption correction.

6.1. Secondary beam fraction

The estimation of the secondary beam fraction is a key point in particular for extended sources analysis. Observations on planets have shown that the real beam (up to 100 arcsec) is larger than pure Gaussian beam by a factor of 1.3. Since angular scales of the order of 180 arcsec and larger are not measured by the NIKA itself, we use the IRAM 30-meter beam pattern (Greve et al. (1998)) to estimate the angular profile of the beam at such scales. In Fig 9, we study the contribution of the far side lobes by measuring the fraction of the beam at different scales and the deviation from a pure gaussian beam. The result of this estimation is presented in Table 1.

6.2. Atmospheric absorption correction using *Skydip* technique

In the previous observation campaigns the atmospheric absorption correction was made using the IRAM tau-meter that performs elevation scans continuously in a fixed azimuthal position at 225 GHz. In order to be able to derive the opacity at the exact position of the scan and at the same frequencies of NIKA we have implemented a procedure in order to use the NIKA instrument itself as a tau-meter. For the last 2012 and 2013 observation campaigns, the NIKA atmospheric calibration has consisted in measuring the variation of the resonances frequencies of the detectors versus the airmass via elevation scans (*skydip*) from 65 to 20 degrees above the horizon. We use that data to calculate the zenith sky opacity (τ) in order to rescale the observed signal (S^{Ground}) onto the scale that would be obtained using a detectors outside the atmosphere (S^{Star}).

We obtain:

$$S^{Star} = S^{Ground} \cdot e^{-x\tau} \quad (4)$$

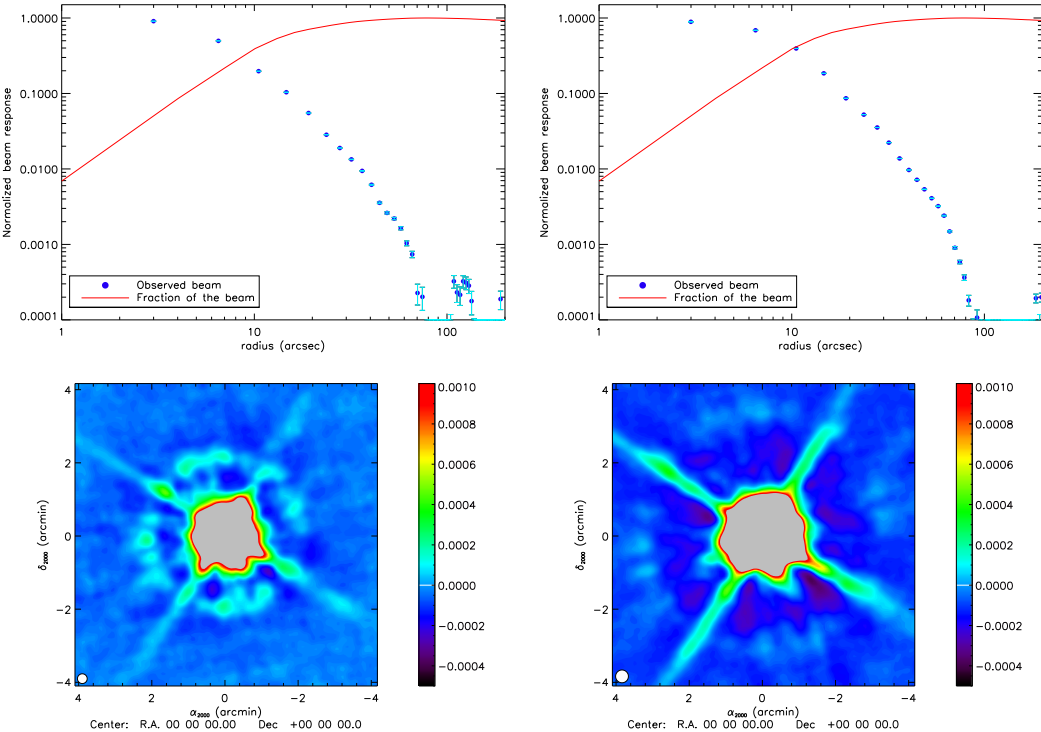


Figure 9. Secondary beam contribution for the 1mm channel (top-left) and 2.14 mm channel (top-right) in the case of Uranus observations. The map of the far side lobes is also presented for 1.25 mm channel (bottom-left) and for 2mm channel (bottom-right): the maps are derived using saturn observation. They show the typical beam pattern of the IRAM 30m telescope (Greve et al. 1998). The spider supporting the secondary mirror of the telescope is visible to a level of about -30 dB.

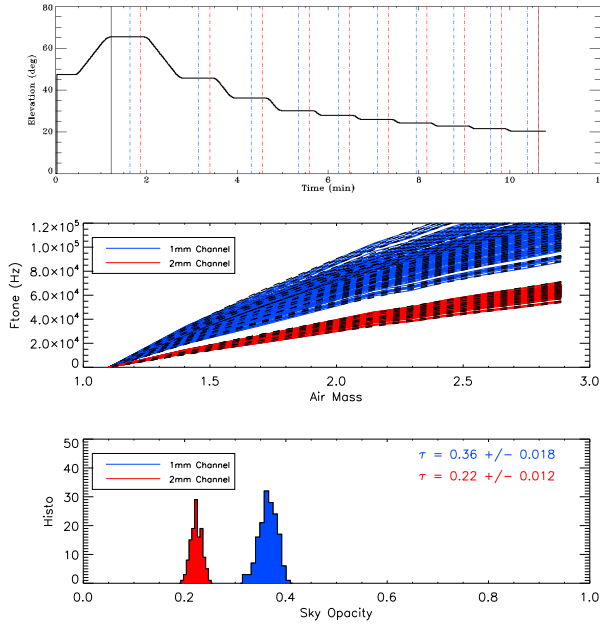


Figure 10. Top plot: telescope positions during an Elevation scan procedure. 10 steps in elevation have been performed without changing the azimuthal position. The useful data for absolute calibration are taken in the region between the blue and the red lines. Middle plot: Bottom plot:

Where $x = \sec(z)$ is the air mass with the zenithal angle $z = \delta$ where δ is the elevation of the telescope.

During a skydip, the telescope performs 10 steps corresponding to 0.18 air mass each. we perform a tuning of the REU before acquiring useful signal. For each step we have 22 seconds useful signal at a given elevation (see Figure 10 in the top).

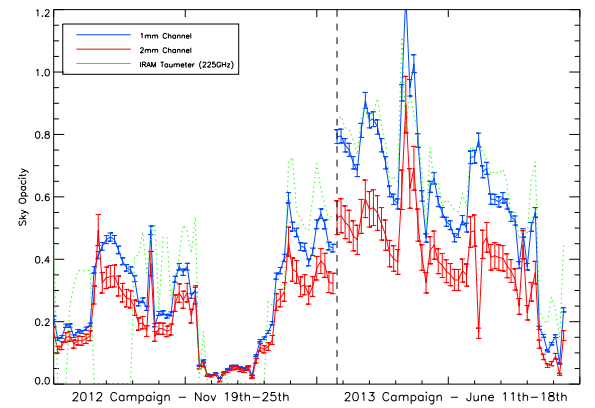


Figure 11. Opacity over the NIKA observational campaigns 2012 and 2013 calculated from the skydips analysis. The errors bars are estimated combining different skydips observations.

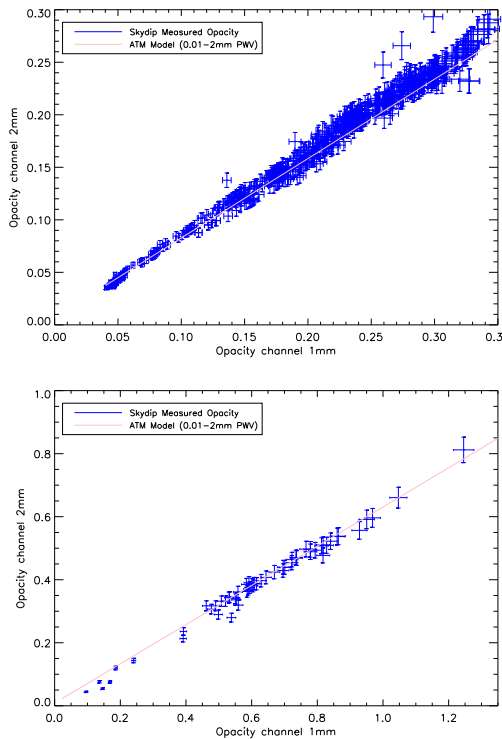


Figure 12. Comparison between the opacities measured with the skydip technique (blue points) and the ATM model (purple lines). top plot is for 2012 campaign; the bottom plot is for 2013 campaign.

We expect the acquired useful signal to respond to the airmass as follows:

$$F_{skydip}^{Ground} = F_0 + CT_{atm}[1 - e^{x\tau_{skydip}}] \quad (5)$$

Here, F_{skydip}^{Ground} is the acquired signal corresponding to the absolute value of the shift in the frequency tone for each pixel. F_0 is the instrumental offset corresponding to the frequency tone excitation for the considered pixel at the beginning of a skydip measurement. C is the calibration conversion factor in Hz/K , T_{atm} (in Kelvin) is the equivalent temperature of the atmosphere and τ_{skydip} is the sky opacity during the skydip. By performing a iterated fit of the 3 parameters F_0 , C and τ , we obtain the sky opacity at zenith during the skydip and in particular the coefficient F_0 and C . In Figures 10 we present the results of the data analysis of one skydip performed during the 2013 campaign.

The F_0 , C coefficients depend only on the response of the detectors; since the non-linearities of the NIKA KIDs are negligible in the considered range of backgrounds, they can be applied to all the observational campaign to recover the opacity of the considered scan. This is obtained by inverting Eq 5 as:

$$\tau_{scan_i} = \frac{1}{x_{scan_i}} \left(1 - \frac{F_{scan_i}^{Ground} - F_0}{CT_{atm}} \right) \quad (6)$$

Where τ_{scan_i} is the opacity of the considered scan, x_{scan_i} correspond to the air mass at the elevation of the considered scan, $F_{scan_i}^{Ground}$ is the absolute value of the frequency tone of the detector during the scan, F_0

and C are the coefficient derived from the skydip technique.

An advantage of this method is that we do not need to perform the skydip at the exact time of the source observations to correct properly the atmospheric contribution in the considered scan. Another advantage, is that we can estimate the opacity at the (AzEl) position of the source, instead of the average sky opacity. This method is limited only by the validity of the air mass scaling law with elevation (secant model) and by the degeneracy of the atmospheric temperature with the opacity in our model. In order no to be too much dependent by this degeneracy we performed few skydips per observational day.

In Fig 11 we present the opacities for all the maps of the NIKA observational campaign 2012 and campaign 2013. During the 2012 campaign on 22th and 23th of November the opacity was less then 0.05 for the 1mm channel. During the 2013 campaign in June the weather was worst permitting to properly observe at 1mm and 2mm channels only for about a day in which the opacity was slightly less then 0.1 at 1mm channel.

6.2.1. Consistency with models

The consistency of the skydip technique can be validate by using the ATM model. We derived the expected opacities integrated into the actual NIKA bandpasses over a range between 0.04 and 20 PWV. In Fig 12 we present the comparison between the opacities derived for 1.24 mm and 2.14 mm (blue point) channels and the ATM model (purple line). The plots in the top present the results for the 2013 observation campaign and the bottom plots for 2013 observation campaign. The agreement between the measured opacities and the model is good for both campaigns.

7. Noise equivalent flux density (NEFD)

The noise equivalent flux density (NEFD) is computed as the array-averaged sensitivity to point-sources *i.e.* the flux rms obtained in one second of integration. The average is done via the reciprocal of the square of the NEFD. It takes into account the time effectively spent by the array on the source.

Figure 13 presents the NEFD for each valid kid of the array at 1.25 mm (top) and 2.14 mm (bottom) obtained during the observation of MM18423+5938. In this case, the average sensitivities on the sky are ~ 48 and $\sim 23 \text{ mJy.s}^{1/2}$ at 1.25 and 2.14 mm respectively. We note that the sensitivity spread across the array is quite large.

Figure 14 presents the array-averaged NEFD of the NIKA camera at 1.25 and 2.14 mm as a function of the line-of-sight opacity $\tau/\sin(\text{el})$, where τ is the zenith opacity and el the elevation. At null zenith opacity, the sensitivities are respectively ~ 40 and $\sim 20 \text{ mJy.s}^{1/2}$ at 1.25 and 2.14 mm, which give an indication of the performance of the 2012 NIKA camera in optimal weather conditions. As expected, the sensitivities degrade with increasing opacity, corresponding to worse weather conditions. At 2.14 mm, we observe just a degradation due to the opacity effect in $\exp(\tau/\sin(\text{el}))$, while at 1.25 mm, the degradation seems to be enhanced. Yet, the sky noise decorrelation seems to work as well in those cases so that we think that the increased power on the kids somehow degrades their performance.

Systematics	1mm Channel Error	2mm Channel Error
Spectral response	2%	1%
Focal plane reconstruction	3.4 arcsec	3.2 arcsec
Secondary beams fraction (cuts at 30°, 60°, 90°)	24.8%, 40.5%, 42.7%	8.8%, 29.7%, 33.2%
Sky subtraction	5%	6.5%

Table 1. Different contributions to the total calibration error of the NIKA data. The secondary beams fraction is estimated with a single gaussian fit.

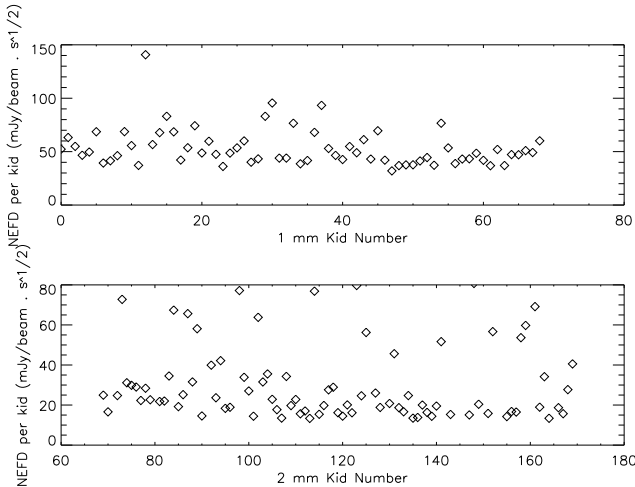


Figure 13. NEFD spread for the two 2012 observation campaign arrays (1.25 mm top, 2.14 mm bottom) measured during the MM18423 scans. The detector sensitivity is shown as a function of the KID number which is sorted according to the resonance frequency. The average NEFD of the two arrays are 48 and 23 mJy.s^{1/2} at 1.25 and 2.14 mm respectively for these observations. If we consider only the best 20% detectors of each array, then we get an average NEFD of 39 and 15 mJy.s^{1/2}

Note that the sensitivity at 1.25 mm was limited by a saturation effect on the readout electronics which has been corrected since. By using only 8 detectors, we were able to detect still the faint source MM18423. In that case, the measured averaged 1.25 mm NEFD is 27 mJy.s^{1/2} which is comparable to MAMBO, the predecessor of NIKA at the 30 m telescope. We think that this sensitivity is representative of the 1.25 mm array, although this is not demonstrated yet.

We note that the flux noise on the SXDF source decreases by 2 (Tab. 2) when going from one to four hours of integration time. This implies that the noise scales as the square root of time at least for the hour timescale.

The 2013 campaign allowed us to test new arrays. Whereas an additional filter limited the 1.25 mm band efficiency, we were able to measure an array sensitivity of 14 mJy.s^{1/2} at 2.14 mm (an improvement by a factor $\frac{1}{3}$ over the 2012 campaign) for the few available hours of good weather.

In conclusion, the NIKA instrument has shown effective average NEFD sensitivities on the sky for point sources of 40 and 14 mJy.s^{1/2} at 1.25 and 2.14 mm in good weather conditions. Yet, the 1 mm channel sensitivity can be expected to be better in the coming observations.

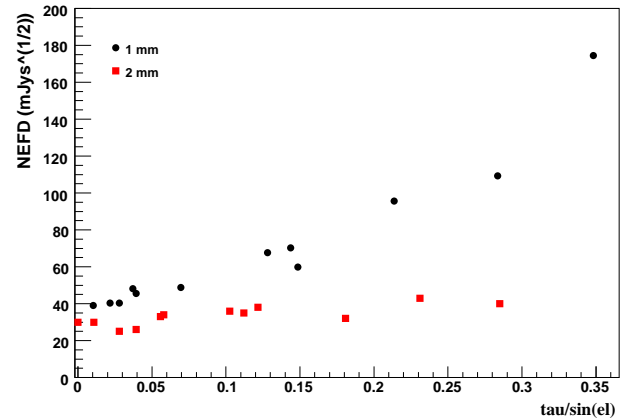


Figure 14. Measured NEFD of the two arrays as a function of $\tau/\sin(\text{el})$, the opacity along the line of sight of the observations. Most of the 1 mm opacity dependence can be attributed to a degradation in the KID resonance quality factor with increasing power load. At 2.14 mm, the trend is compatible with a $\exp(\tau/\sin(\text{el}))$ behavior.



8. NIKA Observations

The NIKA camera has been used during the November 2012 and June 2013 campaigns to observe point-like sources, in order to assess the NIKA photometry, and extended sources to demonstrate the possibility to reconstruct angular scales up to one arcminute.

8.1. Millimetre Spectral Energy Distribution (SED) of selected point sources

Point-like sources have been observed during the good weather conditions in the November 2012 and June 2013 campaigns. They have been selected to be faint but detectable, in order to assess the NIKA photometry with fluxes of the order of few tens of mJy.

Tab. 2 describes the measured point-source fluxes at 1.25 and 2.14 mm. Flux errors are statistical only. The opacity corresponds to a value averaged over the scans. Figure 15 presents the spectral energy distribution (SED) of a selection of four sources observed in 2012 and 2013 campaigns and compares it with previous measurements. We note that NIKA observation ^s are in very good agreement with previous observations. In the following, we discuss the properties of the selected point-sources, that we have chosen amongst high redshift submillimeter galaxies (SMG).

Source name	RA	Dec	$F_\nu(1\text{mm})$	$F_\nu(2\text{mm})$	T_{int}	$\tau_{1\text{mm}}$	$\tau_{2\text{mm}}$
	2000	2000	mJy	mJy	min		
HLS091828	09:18:28.600	+51:42:23.300	36.7 ± 4.6	8.3 ± 0.7	83	0.27	0.22
MM18423*	18:42:22.500	+59:38:30.000	29 ± 4	5.5 ± 0.7	56	0.02	0.01
MM18423	18:42:22.500	+59:38:30.000	33.6 ± 3	6.3 ± 0.8	37	0.02	0.03
MM18423 ^{r6}	18:42:22.500	+59:38:30.000	20 ± 2	4.3 ± 0.3	26	0.56	0.34
SXDF	02:18:30.600	-05:31:30.000	20 ± 3	4.1 ± 0.8	68	0.02	0.02
SXDF	02:18:30.600	-05:31:30.000	28 ± 1.5	4.1 ± 0.4	258	0.03	0.03
HFLS3 ^{r6}	17:06:47.800	+58:46:23.000	16 ± 2	4.0 ± 0.6	16	0.14	0.07
Arp220	15:34:57.100	+23:30:11.000	243 ± 3	52.8 ± 0.8	47	0.11	0.09
HAT084933	08:49:33.400	+02:14:43.000	13 ± 3	1.3 ± 0.8	59	0.08	0.07
HAT133008	13:30:08.560	+24:58:58.300	16 ± 3	4.5 ± 0.8	55	0.14	0.10
PSS2322+1944	23:22:07.200	+19:44:23.000	< 4.6	< 1.7	57	0.06	0.05
GRB121123A	20:29:16.290	-11:51:35.900	< 15	< 1.7	69	0.22	0.18
4C05.19	04:14:37.800	+05:34:42.000	< 17	< 2.5	15	0.13	0.11
ZZTauIRS	04:30:51.714	+24:41:47.510	77 ± 2	16.2 ± 0.8	40	0.01	0.00
CXtau	04:14:47.865	+26:28:11.010	< 4.6	< 1.7	40	0.02	0.01

Table 2. NIKA Flux and sensitivity of a collection of point sources. The integration time is given in minutes. The average zenith opacities are given in the last two columns. Upper limits are given as 2σ . Most of the data were taken from the 19th to the 24th of November 2012. SXDF field was observed twice (22nd and 23rd of November 2012). * Data taken with a different setting (8 Kids only at 1mm). ^{r6} Data taken in June 2013.

MM18423+5938

MM18423+5938 is a submillimeter galaxy at $z = 3.93$ discovered serendipitously (Lestrade et al. (2009)) in a search for cold debris disks around M-dwarfs with MAMBO-2 at the IRAM 30-m millimeter telescope. Flux densities at 1.2 mm, 2 mm and 3 mm have been measured (Lestrade et al. (2010)). The relatively high flux (about 30 mJy at 1 mm) is explained by the fact that this SMG is gravitationally lensed, as can be assessed by the observation of the CO emission which is consistent with a complete Einstein ring with a major axis diameter of 1.4'' (Lestrade et al. (2011)). J. P. McKean et al. have fitted the SED with a single temperature modified blackbody spectrum, with $\beta = 1.5 \pm 0.5$ and $T = 24^{+7}_{-5}$ K, although the lack of measurements at high frequencies allows for a larger range of temperatures (McKean et al. (2011)). Figure (upper left) presents the SED of MM18423+5938 with NIKA measurements, that are in good agreement. The source has been measured during the 2013 campaign as well. It shows the same flux at 2 mm within 2σ . The discrepancy at 1 mm is likely due to the different bandpasses and the mediocre weather at the time of the observations. We suspect that anomalous refraction (Altenhoff et al. (1987)), which tends to broaden the effective beams, has diluted the measured flux at that time.

HLSJ091828.6+514223

HLSJ091828.6+514223 is an exceptionally mm and submm bright source discovered behind the $z=0.22$ cluster Abell 773 (Combes et al. (2012)). It appears to be a strongly lensed submillimeter galaxy (SMG) at a redshift of $z=5.24$, the lens being an optical source lying in the neighborhood. It has been measured at 2 mm (IRAM-30 m EMIR), 1.3 mm (SMA) and 0.88 mm (SMA), see (Combes et al. (2012)) and references therein. Figure (upper left) presents the SED of HLSJ091828.6+514223 with NIKA measurements.

SXDF1100.001

SXDF1100.001 (also known as Orochi) is an extremely bright (50 mJy at 1 mm) submillimeter galaxy, discovered in 1.1 mm observations of the Subaru/XMM-Newton Deep Field using AzTEC on ASTE (Ikarashi et al. (2011)). It is believed to be a lensed, optically dark SMG lying at $z=3.4$ behind a foreground, optically visible (but red) galaxy at $z=1.4$.

Continuum flux densities at millimeter wavelengths have been measured by SMA, Carma, Z-SPEC/CSO and AzTEC/ASTE, see (Ikarashi et al. (2011)) and references therein. Figure (lower left) presents the SED of SXDF1100.001 with NIKA measurements. To our knowledge, this is the first measurement in the 2 mm band.

HFLS3

HFLS3 has been reported as a massive starburst galaxy at redshift 6.34 (Riechers et al. (2013)). Continuum emission has been measured over a large wavelength range, in particular at millimeter wavelengths (Z-Spec, PdBI, CARMA, Gismo), see (Riechers et al. (2013)) and references therein. Figure (lower right) presents the SED of HFLS3 with NIKA measurements, that are in good agreement.

These four comparisons of NIKA observations at 1 and 2 mm with previous observations allow us to assess the NIKA photometry. Other observations allow to probe the diversity of sources and fluxes and measure the camera performance in various background conditions.

8.2. Mapping of extended sources

During the 2012 and 2013 observation campaigns we have observed simultaneously at 1 and 2 mm several well-known extended sources to test the capabilities of the NIKA camera to recover large angular scales up to 5 arcmin. We performed both elevation and azimuth raster scans to ensure an homogeneous coverage of the mapped area. The size of the scans and integration time have been adapted to

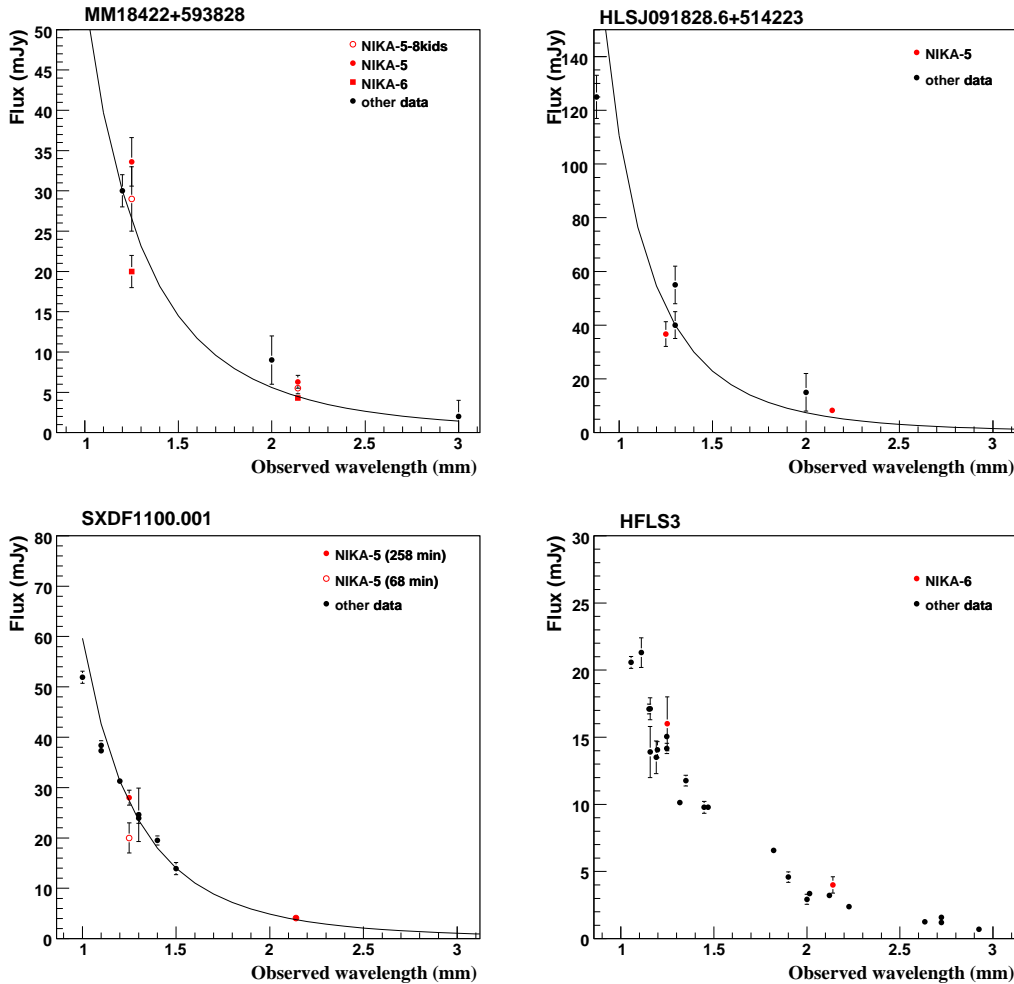


Figure 15. SED of selected pointlike sources observed with NIKA-5/NIKA-6, flux (mJy) as a function of the observed wavelength (mm). Upper left : MM18422+593828 observed by NIKA-5 (red points) and previous millimeter observations (black points) (Lestrade et al. (2010)). Solid line indicates a modified grey body with $\beta = 1.5$ and $T = 24$ K, see (McKean et al. (2011)). Upper right : HLSJ091828.6+514223 observed by NIKA-5 (red points) and previous millimeter observations (black points), see (Combes et al. (2012)) and references therein. Lower left : SXDF1100.001 observed by NIKA-5 (red points) and previous millimeter observations (black points), see (Ikarashi et al. (2011)) and references therein. Lower right : HFLS3 observed by NIKA-5 (red points) and previous millimeter observations (black points), see (Riechers et al. (2013)) and references therein.

each source. We present three examples of extended sources, namely the Horsehead Nebula, the Cygnus A and DR21 OH regions that have been observed during the 2012 campaign. The center pointing position, the size of the scans and the integration time for each sources are given in Table 3. We also present the median rms of the map and atmospheric opacity for the 1.25 and 2.14 mm maps.

The Horsehead nebula

The Horsehead nebula is a close-by (400 pc) dark protrusion emerging from its parental cloud L1630 in the Orion B molecular complex. This condensation is illuminated by the 09.5V star σ Ori (distance 0.5° from the cloud) and presents a Photon-Dominated Region (PDR) on its western side seen perfectly edge-on (Abergel et al. 2003).

We concentrate here in the outer neck (Hily-Blant et al. 2005) which consists of the PDR, the nose, the mane and

the jaw. In the top raw of Figure 16 we show the 1.25 (left) and 2.05 (middle) mm NIKA maps. The typical rms of the noise in the maps is of 14.5 and 2 mJy/beam at 1.25 and 2.05 mm, respectively. The NIKA 1.25 mm is consistent with the 1.2 mm continuum map (Hily-Blant et al. 2005) obtained with MAMBO2, the MPIfR 117-channel bolometer array (Kreysa 1992). We clearly observe in the NIKA maps the PDR region whose morphology changes significantly from one frequency to another. This is also obvious in the spectral index map presented in the right figure. The northern part of the PDR presents a significantly flatter spectral index (about 2.4) than the southern part and the mane (about 4.5). Two possible explanations are: CO 2-1 contamination at 1 mm and/or high dust emissivity spectral index. There are some evidence 2 mm only emission regions that might be due to free-free emission.

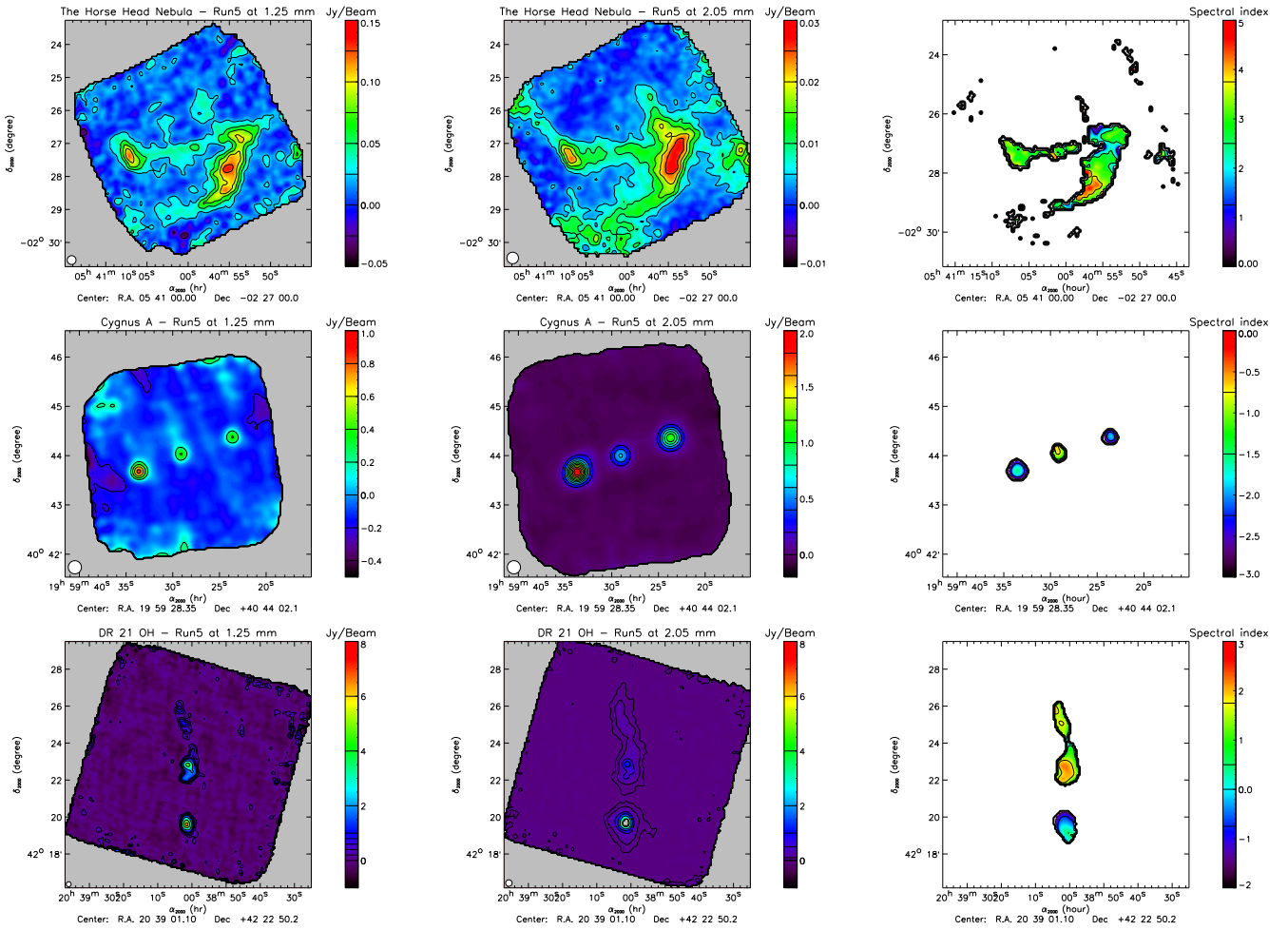


Figure 16. Examples of 1.25 (left) and 2.05 (middle) NIKA maps of well-known extended sources. From top to bottom we present the Horsehead nebula, the Cygnus A galaxy including the central source and the hot spots, and the DR21 OH complex. Spectral index maps are presented on the left column.

Source	RA	DEC	Integration Time	Noise rms 1.25 mm	Noise rms 2.05 mm	τ_{1mm}	τ_{2mm}
	[deg]	[deg]	[arcmin]	[s]	[mJy/beam]	[mJy/beam]	
Horsehead	85.25	-2.45	1.57	14.5	2.0	0.027	0.022
Cygnus A	299.86	40.73	0.61	76.3	28.9	0.15–0.34	0.12–0.33
DR 21 OH	309.75	16.27	0.54	181.0	12.6	0.27	0.22

Table 3. Main properties of the maps of extended sources: center of the map, size of the scan, integration time, rms noise and opacity at the two observation frequencies.

Cygnus A

Cygnus A is locally the most powerful Fanaroff- Riley II (FRII) radio galaxy, and therefore it is also the best studied in terms of spatial resolution. It lies at a distance of 227 Mpc. The global properties of the object are well reviewed in the literature (Carilli & Harris 1996). In terms of synchrotron emission at low radio frequencies, the two giant lobes dominate the emission (Hargrave & Ryle 1974), but at higher frequencies the hotspots, or working surfaces in the lobes, become more prominent along with the galaxy core. The southern and northern hotspots are respectively 50 and 70 arcsec from the core.

The NIKA maps of Cygnus A at 1.25 (left) and 2.05 (middle) mm are presented in the middle row of Figure 16. The typical rms of the map is of 76 and 29 mJy/beam at 1.25 and 2.05 mm, respectively. As expected, the two hot spots and the galaxy core dominate the signal at the NIKA frequencies. The hot spots present a spectral index (right map on the row) in the range from -1.5 to -2.0, which is consistent with synchrotron emission but steeper than the value found by Robson et al. (1998), which is ~ -1 . The galaxy core shows a flatter spectrum from -0.6 to -1.0, which is consistent with previous estimates from Leeuw & Robson (1999).

DR21 complex

The giant star-forming complex, DR21 is located in the constellation Cygnus at ~ 3 kpc from Earth (Campbell et al. 1982). H₂O masers (Genzel & Downes 1977) and a map of the 1.3-mm continuum emission (Motte et al. 2005) show that DR21 belongs to a north-south orientated chain of massive star forming complexes. DR21 is composed from north to south of three main regions DR21, DR21 OH and DR21 Main (DR21M). DR21M has a mass of ~ 20000 M $_{\odot}$ and contains one of the most energetic star forming outflows detected (Garden et al. 1991a,b; Garden & Carlstrom 1992).

We present in the bottom row of Figure 16 the NIKA maps of the DR21 complex at 1.25 (left) and 2.05 (right) mm. We observe in those the three main regions in the complex, the most intense being DR21OH and DR21M. As shown in the right plot of the row, the spectral characteristics of these two regions are significantly different. DR21M has a flatter spectrum in the frequency range of NIKA. We suspect the presence of strong free-free emission.

9. Conclusion and Perspectives

In this paper we have shown that *NIKA* is a competitive instrument for millimeter wave astronomy using KID detector technology. We obtained a sensitivity (averaged over all valid detectors) of 40 and 14 mJy.s^{1/2} for best weather conditions for the 1.25 mm and 2.14 mm arrays respectively estimated on point-like sources.

We have presented several instrumental and data analysis improvements. In particular some of the major aspects that limited the calibration accuracy of *NIKA* were the real time optimisation of the detectors working point and the atmospheric absorption correction. These improvements have been described in this work with a discussion about how these technical improvements permitted to reach astrophysical quality data by presenting results obtained for several astrophysical point like and extended sources.

The final *NIKA* 2 will be made of about 1000 detectors at 2.14 mm and 4000 at 1.24 mm with a field of view of ~ 6.5 arcmin. *NIKA* 2 will be commissioned at the end of 2015. In addition the NIKA collaboration opened to host a polarised 1.24 mm array in the final *NIKA* 2 instrument. The performance in polarisation will be tested in the *NIKA* camera during 2014 observation campaigns.

Acknowledgements. We would like to thank the IRAM staff for their support during the campaign. This work has been partially funded by the Foundation Nanoscience Grenoble, the ANR under the contracts "MKIDS" and "NIKA". This work has been partially supported by the LabEx FOCUS ANR-11-LABX-0013. This work has benefited from the support of the European Research Council Advanced Grant ORISTARS under the European Union's Seventh Framework Programme (Grant Agreement no. 291294). The NIKA dilution cryostat has been designed and built at the Institut Néel. In particular, we acknowledge the crucial contribution of the Cryogenics Group, and in particular Gregory Garde, Henri Rodenas, Jean Paul Leggeri, Philippe Camus.

References

- Abergel, A., Teyssier, D., Bernard, J. P., et al. 2003, A&A, 410, 577
 Altenhoff, W. J., Baars, J. W. M., Wink, J. E., & Downes, D. 1987,
 A&A, 184, 381
- Barends, R., Baselmans, J. J. A., Yates, S. J. C., et al. 2008, Physical Review Letters, 100, 257002
 Bourrion, O., Vescovi, C., Bouly, J. L., et al. 2012a, in Society of Photo-Optical Instrumentation Engineers (SPIE) Conference Series, Vol. 8452, Society of Photo-Optical Instrumentation Engineers (SPIE) Conference Series
 Bourrion, O., Vescovi, C., Bouly, J. L., et al. 2012b, Journal of Instrumentation, 7, 7014
 Calvo, M., Roesch, M., Désert, F. X., et al. 2013, Astronomy and Astrophysics, 551, L12
 Campbell, M. F., Niles, D., Nawfel, R., et al. 1982, ApJ, 261, 550
 Carilli, C. L. & Harris, D. E. 1996, Cygnus A – Study of a Radio Galaxy
 Combes, F., Rex, M., Rawle, T. D., et al. 2012, A&A, 538, L4
 Doyle, S., Naylor, J., Mauskopf, P., Porch, A., & Dunscombe, C. 2007, in Eighteenth International Symposium on Space Terahertz Technology, ed. A. Karpov, 170
 Garden, R. P. & Carlstrom, J. E. 1992, ApJ, 392, 602
 Garden, R. P., Geballe, T. R., Gatley, I., & Nadeau, D. 1991a, ApJ, 366, 474
 Garden, R. P., Hayashi, M., Hasegawa, T., Gatley, I., & Kaifu, N. 1991b, ApJ, 374, 540
 Genzel, R. & Downes, D. 1977, A&AS, 30, 145
 Hargrave, P. J. & Ryle, M. 1974, MNRAS, 166, 305
 Hily-Blant, P., Teyssier, D., Philipp, S., & Güsten, R. 2005, A&A, 440, 909
 Ikarashi, S., Kohno, K., Aguirre, J. E., et al. 2011, MNRAS, 415, 3081
 Kreysa, E. 1992, in ESA Special Publication, Vol. 356, Photon Detectors for Space Instrumentation, ed. T. D. Guyenne & J. Hunt, 207–210
 Leeuw, L. L. & Robson, E. I. 1999, in IAU Symposium, Vol. 194, Activity in Galaxies and Related Phenomena, ed. Y. Terzian, E. Khachikian, & D. Weedman, 179
 Lestrade, J.-F., Carilli, C. L., Thanjavur, K., et al. 2011, ApJ, 739, L30
 Lestrade, J.-F., Combes, F., Salomé, P., et al. 2010, A&A, 522, L4
 Lestrade, J.-F., Wyatt, M. C., Bertoldi, F., Menten, K. M., & LaBraga, G. 2009, A&A, 506, 1455
 McKean, J., Alba, A. B., Volino, F., et al. 2011
 Monfardini, A., Deesert, F.-X., Ponthieu, N., et al. 2012, GRB Coordinates Network, 14088, 1
 Motte, F., Bontemps, S., Schilke, P., et al. 2005, in IAU Symposium, Vol. 227, Massive Star Birth: A Crossroads of Astrophysics, ed. R. Cesaroni, M. Felli, E. Churchwell, & M. Walmsley, 151–156
 Pardo, J. R., Cernicharo, J., & Serabyn, E. 2002, IEEE, 49, 1683
 Planck Collaboration, AMI Collaboration, Ade, P. A. R., et al. 2013, A&A, 550, A128
 Riechers, D. A., Bradford, C. M., Clements, D. L., et al. 2013, Nature, 496, 329
 Robson, E. I., Leeuw, L. L., Stevens, J. A., & Holland, W. S. 1998, MNRAS, 301, 935
 Roesch, M., Benoit, A., Bideaud, A., et al. 2012, ArXiv e-prints
 Swenson, L. J., Cruciani, A., Benoit, A., et al. 2010, Applied Physics Letters, 96, 263511
 Tauber, J. A. & Planck Collaboration. 2012, Mem. Soc. Astron. Italiana, 83, 72